

Reactionless Camera Inspection With a Free-Flying Space Robot Under Reaction Null-Space Motion Control

Hiroki Sone^a, Dragomir Nenchev^{a,*}

^a*Graduate School of Engineering, Tokyo City University, Tamazutsumi 1-28-1, Setagaya-ku, Tokyo 158-8557, Japan*

Abstract

The possibility of implementing reactionless motion control w.r.t. base orientation of a free-flying space robot in practical tasks is addressed. It is shown that such possibility depends strongly on the kinematic/dynamic design parameters as well as on the mission task. A successful implementation of a camera inspection task is reported. The presence of kinematic redundancy and the manipulator attachment position are shown to play important roles. More specifically, for a manipulator arm with a typical seven degree-of-freedom (DoF) kinematic structure, it is shown that two motion patterns, wrist reorientation and folding/unfolding of the arm, result in almost reactionless motion. The orientation pattern is adopted as the main task for camera inspection, while the remaining four DoFs are used to ensure complete reactionless motion and to minimize the position errors. Since the composition of these tasks introduces the so-called algorithmic singularities, **two methods** are suggested to alleviate the problem. Furthermore, it is shown that other types of singularities may also be introduced in case of an inappropriate choice of the manipulator attachment position. At the end, numerical analysis is provided to show that reactionless motion provides an advantage in terms of kinetic energy as well.

Keywords: Free-flying space robot, Reactionless motion control, Practical application

1. Introduction

The development of free-flying space robots (FFSR) has been steadily advancing since their first appearance about almost three decades ago [1]. These robots are envisioned to perform a few sophisticated space missions such as space debris removal, repairing/refueling of satellites and construction of large space structures [2]. A FFSR comprises a satellite base with attitude control devices, such as reaction wheels, and one or more manipulator arms. The controller has to deal with base rotation arising from the dynamic coupling between the manipulator(s) and the floating satellite base [3]. Because of the base rotation, control methods which are used in terrestrial manipulators cannot be directly applied.

One possible approach to solve the above problem is to implement a controller based on the Generalized Jacobian [4]. Thereby, the momentum conservation law is used as a constraint to eliminate the base rotation resulting from the differential relationships in the system. Thus, similar to terrestrial robots, the end-effector velocity can be represented in terms of joint velocity only, without the need of base angular velocity/acceleration measurement. Methods of analysis and control developed for terrestrial robots can then be implemented by replacing the fixed-base Jacobian matrix with the generalized one [5, 6].

*Corresponding author. Tel.: +81 357072108.

Email address: nenchev@tcu.ac.jp (Dragomir Nenchev)

On the other hand, ignoring base rotation becomes a significant issue as it leads to communication problems with the ground control center. Note that the admissible base attitude variation during the Japanese Engineering Test Satellite VII (ETS-VII) mission was just ± 0.05 deg. In general, attitude control devices such as reaction wheels, are employed to compensate the undesirable base attitude variation [7, 8]. However, this approach has limited capabilities when the base attitude disturbance stems from manipulator motion [9]. To avoid saturation of the reaction wheel signals, the manipulator has to be driven at very low speed. Note however, that in the case of repeatable tasks, e.g. observation/inspection or assembly for construction missions, low speed manipulation might not be desirable from the viewpoint of work efficiency. Therefore, the dynamic coupling and manipulator reaction control problems are considered as important as the end-effector motion/force control.

A pioneering work on FFSR manipulator reaction control introduced the Disturbance map concept [10, 11]. The base disturbance magnitude/direction is visualized as a colored map in joint space. With this tool, low reaction paths can be obtained in an intuitive manner. However, it is difficult to employ the method when using manipulators with more than two DoFs. Another approach to the reaction minimization problem is provided by the Reaction Null-Space (RNS) method [12, 13, 14]. Reactionless motion generation is obtained in a straightforward manner, thus avoiding the shortcoming of the Disturbance map. Paths, generated offline via the RNS method, have been successfully executed as an on-orbit experiment during the extended ETS-VII mission [15, 16]. After the mission, RNS-based reactionless motion generation and control have been examined by several researchers [17, 18, 19, 20]. Angular momentum distribution control for capturing non-cooperative satellites under RNS control was proposed in [21, 22]. Reactionless motion control during a debris removal task with a planar dual-arm system was investigated in [23]. Recently, the method has also been considered as a component in vibration control of systems with flexible appendages [24].

A shortcoming of the RNS method is that reactionless motions are confined to a reactionless manifold in joint space that depends on the initial state. Another shortcoming is the occurrence of singularities that differ from those appearing in the inverse kinematics of terrestrial manipulators¹. This limits the application of the method in quite a conservative way, such that general end-effector path tracking tasks cannot be performed. Indeed, within the extended ETS-VII mission, only predefined reactionless paths have been examined [15, 16]. Efforts have been undertaken since to broaden the scope of the method. One possible approach is to take advantage of kinematic redundancy. Note that the reactionless motion control task requires a manipulator arm with at least nine DoFs: six DoFs for the end effector task plus three-DoFs for base rotation. Another possibility is to use a dual arm manipulator system [26, 27]. Nevertheless, the results obtained so far have shown that reactionless *position-based* end-effector path tracking, requiring large variations in the joint variables, is quite limited, even if singularity treatment techniques are used.

Based on the above analysis, it can be concluded that an *orientation-based* path tracking task might be a good candidate for the practical implementation of reactionless motion control. So far, such tasks have not been considered by others. In this work, we examine a hand-held camera inspection task to be performed by a manipulator arm with seven DoFs [28]. A seven-DoFs manipulator arm is assumed to be a good choice in various space missions, e.g. the Restore Robot Arm mission [25]. Such arm comprises one *degree of redundancy* w.r.t. the end-effector and base rotation tasks, each of them requiring three-DoFs. Structure-specific motion analysis is performed to identify motion patterns (or synergies) that yield prevailing reactionless motion. It will become apparent that the reactionless motion sets for this arm can

¹The latter are known as kinematic singularities, while the former include dynamic singularities [11, 25] as well as the so-called “algorithmic singularities.”

be represented as a superposition of two specific motion patterns: predominant wrist motion and arm folding/unfolding motion. Based on this result, we pick up the predominant wrist motion to realize the camera inspection task. The analysis also reveals that the manipulator attachment position may play an important role in addition to that of the kinematic redundancy. At the end of the study, we show that besides the main advantage (of base attitude disturbance minimization), reactionless motion provides another advantage in relation to instantaneous kinetic energy minimization. A comparative numerical analysis study is presented whereby the same task is performed under conventional inverse-Jacobian control plus attitude disturbance control with the help of a set of three reaction wheels.

This paper is organized as follows. In the following section we describe the background of the work: the momentum conservation law and the Reaction Null Space projection. In Section 3, we present the manipulator model and provide a representation of its reactionless motion. In addition, analysis is performed to identify the role of the manipulator attachment position w.r.t. reactionless motion. In Section 4, we introduce the main equation for reactionless motion generation and control during the camera inspection task. Numerical simulations demonstrate the capabilities of the proposed method, when compared to the inverse Jacobian controller. In Section 5, algorithmic singularity analysis is provided. Results from the comparative analysis in terms of kinetic energy are presented in Section 6. Finally, the conclusions are given in Section 7.

2. A brief review of reactionless motion control

2.1. Angular momentum conservation law

We consider a FFSR model consisting of a satellite base and a serial manipulator arm with n -DoF. In space environment, it is known that linear and angular momenta are conserved when there is no external force. Actually, the gravity gradient torque and solar radiation force violate this conservation. However, since the duration time of space robot missions is relatively short, we can assume that the momenta are conserved.

For a system with 3-axis reaction wheels, the momenta are expressed as follows [21, 22]:

$$\begin{bmatrix} \mathbf{p} \\ \mathbf{l}_b \end{bmatrix} = \begin{bmatrix} \mathbf{M}_v & \mathbf{M}_{v\omega} \\ \mathbf{M}_{v\omega}^T & \mathbf{M}_\omega \end{bmatrix} \begin{bmatrix} \mathbf{v}_b \\ \boldsymbol{\omega}_b \end{bmatrix} + \begin{bmatrix} \mathbf{M}_{vm} \\ \mathbf{M}_{\omega m} \end{bmatrix} \dot{\boldsymbol{\theta}} + \begin{bmatrix} \mathbf{M}_{vr} \\ \mathbf{M}_{\omega r} \end{bmatrix} \dot{\boldsymbol{\phi}} \quad (1)$$

where $\mathbf{p}, \mathbf{l}_b \in \mathbb{R}^3$ denote constant linear and angular momentum w.r.t. the center of mass (CoM) of the base, $\mathbf{v}_b, \boldsymbol{\omega}_b \in \mathbb{R}^3$ stand for linear and angular velocity of the base, and $\dot{\boldsymbol{\theta}} \in \mathbb{R}^n$ and $\dot{\boldsymbol{\phi}} \in \mathbb{R}^3$ are the joint velocity and the reaction wheel velocity vectors, respectively. $\mathbf{M}_v, \mathbf{M}_{v\omega}, \mathbf{M}_\omega \in \mathbb{R}^{3 \times 3}$ are submatrices of the composite-rigid-body (CRB) inertia matrix, $\mathbf{M}_{vm}, \mathbf{M}_{\omega m} \in \mathbb{R}^{3 \times n}$ denote inertia submatrices related to the dynamic coupling between the base and the manipulator. $\mathbf{M}_{vr}, \mathbf{M}_{\omega r} \in \mathbb{R}^{3 \times 3}$ denote inertia matrices related to the dynamic coupling between the base and the reaction wheels.

For a FFSR, the angular momentum conservation law, especially, is of prime importance. Indeed, it has been noted that even slight variations of the base attitude may cause a failure in the communication between the robot and the ground control center. From (1), eliminate velocity \mathbf{v}_b to obtain the following form of the angular momentum conservation law (under the assumption of zero initial momentum):

$$\tilde{\mathbf{M}}_\omega \boldsymbol{\omega}_b + \tilde{\mathbf{M}}_{\omega m} \dot{\boldsymbol{\theta}} + \tilde{\mathbf{M}}_{\omega r} \dot{\boldsymbol{\phi}} = \mathbf{0} \quad (2)$$

where the notation $(\tilde{\circ})$ represents a quantity that includes the base linear motion effect: $\tilde{\mathbf{M}}_\omega = \mathbf{M}_\omega - \mathbf{M}_{v\omega}^T \mathbf{M}_v^{-1} \mathbf{M}_{v\omega}$, $\tilde{\mathbf{M}}_{\omega m} = \mathbf{M}_{\omega m} - \mathbf{M}_{v\omega}^T \mathbf{M}_v^{-1} \mathbf{M}_{vm}$ and $\tilde{\mathbf{M}}_{\omega r} = \mathbf{M}_{\omega r} - \mathbf{M}_{v\omega}^T \mathbf{M}_v^{-1} \mathbf{M}_{vr}$. In the above equation, the first term on the r.h.s. is the partial angular momentum stemming from base

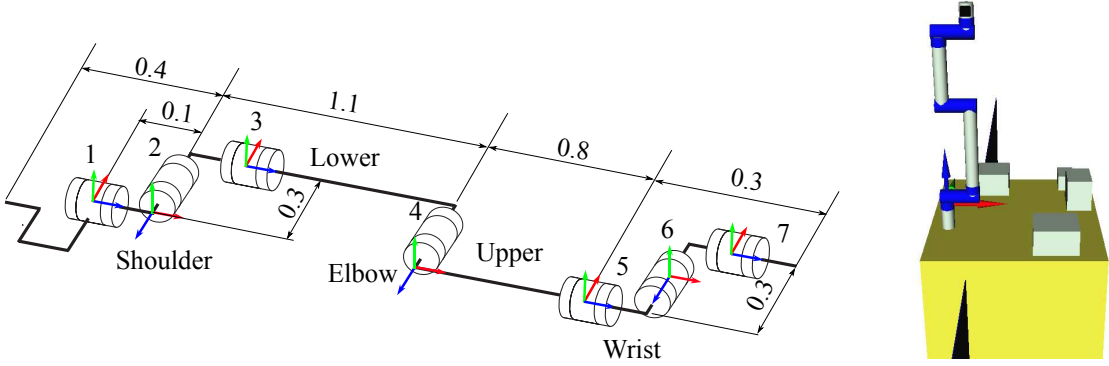


Figure 1: The seven-DoF manipulator model is shown at its initial configuration ($\theta_i = 0$, $i = \overline{1, 7}$).

rotation. The second term results from manipulator motion: it represents the base disturbance in terms of momentum and is referred to as the *coupling angular momentum*. Matrix $\tilde{\mathbf{M}}_{\omega m}$, appearing in this term, will be referred to as the coupling inertia matrix [21]. Finally, the third term represents the angular momentum stored in the reaction wheels. Note that until Section 6, the system is regarded as free-floating ($\dot{\phi} = \mathbf{0}$). For the sake of simplicity, zero initial momenta are assumed without losing generality, hereafter.

2.2. Reaction Null-Space

Reactionless motion is determined by variations of the manipulator configuration that conserve a zero initial base angular momentum throughout the entire motion. This implies $\boldsymbol{\omega}_b = \mathbf{0}$, and hence,

$$\tilde{\mathbf{M}}_{\omega m} \dot{\boldsymbol{\theta}} = \mathbf{0}. \quad (3)$$

From this equation, the set of reactionless motion can be represented as [14]:

$$\dot{\boldsymbol{\theta}} = \mathbf{P}_{RNS} \dot{\boldsymbol{\theta}}_a, \quad (4)$$

where $\mathbf{P}_{RNS} = \mathbf{E} - \tilde{\mathbf{M}}_{\omega m}^+ \tilde{\mathbf{M}}_{\omega m} \in \mathbb{R}^{n \times n}$ denotes a projector onto the null-space of the coupling inertia matrix, $\mathbf{E} \in \mathbb{R}^{n \times n}$ is the identity matrix and $(\circ)^+$ stands for the pseudoinverse matrix. $\dot{\boldsymbol{\theta}}_a \in \mathbb{R}^n$ is an arbitrary vector with the dimension of joint velocity. It plays the role of a vector-parameter w.r.t. the set of reactionless motion. It is apparent that the null-space of the coupling inertia matrix, referred henceforth as the *Reaction Null-Space* (RNS), plays an important role for reactionless motion generation. It should be noted that the entire set of reactionless motion can be represented with the above notation. Hence, zero reaction motion generated by other methods, such as nonlinear optimization programming for example, is identical with that obtained from (4).

3. Space robot model and reactionless motion analysis

3.1. Reactionless motion patterns with a seven-DoF manipulator model

We consider a FFSR model consisting of a satellite base and a seven-DoF serial-link kinematically redundant manipulator. The manipulator is characterized by a kinematic chain with a distinctive lower/upper arm subchain, including a rotational “elbow” joint, a “shoulder” and a “wrist” joint. The structure is characterized with offsets at these joints such that the arm can be folded and stowed during liftoff. The kinematic structure and simulation model are displayed in Fig. 1. The manipulator attachment position is determined from the ETS-VII design, at $[-0.79 \ -0.29 \ 1.0]^T$ m with respect to the base CoM coordinate frame [9]. The dynamic model parameters are shown in Table 1.

Table 1: Dynamic model parameters

	Mass [kg]	Inertia moment [kgm ²]		
<i>i</i>	m_i	I_{xi}	I_{yi}	I_{zi}
<i>b</i>	2552	6200	3540	7090
1	30.0	0.0671	0.0671	0.0851
2	30.0	0.0843	0.267	0.267
3	45.0	3.81	3.81	0.127
4	40.0	0.113	2.19	2.19
5	20.0	0.213	0.213	0.0250
6	20.0	0.0250	0.0292	0.0292
7	25.0	0.0990	0.0990	0.0313

We proceed with the identification of reactionless motion capability pertinent to this manipulator model. This will be done in an intuitive way, based on the properties of the kinematic structure. First, note that the DoF of reactionless motion is four. This number is obtained as the difference between the number of joints (seven) and the base attitude variables (three). Next, note that in manipulator structural analysis usually the kinematic chain is divided into two subchains: the positioning subchain comprising Joints 1 through 4, and the wrist subchain comprising the rest of the joints. The main role of the positioning subchain is to place the wrist within the workspace at a desired location. The main role of the wrist, on the other hand, is to ensure the desired orientation of the end effector. The wrist subchain is characterized by a relatively small mass/inertia. Hence, the angular momentum produced by the motion of the wrist subchain will be far smaller than that obtained from the positioning subchain. Therefore, we can assume that subtle motion in the positioning subchain has the capability to compensate the base disturbance induced by the wrist subchain motion. Exceptions are special (singular) configurations of the positioning subchain. We obtain then a distinctive three-DoF reactionless motion pattern, characterized with “unconstrained” wrist motion plus subtle compensating motion in the positioning subchain, as shown in Fig. 2 (a). This pattern will be henceforth referred to as *predominant wrist motion*. The remaining one-DoF reactionless motion pattern is obtained by rotating the upper/lower arms of the positioning subchain in opposite directions, such that the respective reaction torques cancel out. This is accomplished by rotations in Joints 2 and 3, at the shoulder and the elbow, respectively. Note that the reaction torque generated by these joints is substantially different: Joint 3 generates a much smaller reaction than Joint 2. This becomes apparent from momentum conservation equation (3), since the mass/inertia coefficients for Joint 3 are much smaller than those for Joint 2. Hence, to compensate the reaction torque generated by Joint 3, only a subtle motion in Joint 2 would be sufficient. This behavior will also be confirmed via simulation with a simple 2R FFSR model in the following section. The Joint 2/3 motion pattern is characterized as a predominant elbow folding/unfolding motion (see Fig. 2 (b)).

In addition to the expected subtle (compensating) motion in Joint 2 during the above identified two reactionless motion patterns, we can expect that the motion in Joint 1 will also be subtle and compensating only; none of the above patterns require active involvement of Joint 1. We can then arrive at the following conclusion: because the end-effector position largely depends on the motion in the positioning subchain, it follows that under reactionless motion, the positioning DoF of the end effector can be assumed to be just one. This DoF is determined mainly by the elbow folding/unfolding pattern. This is a severe limitation with regard to general positioning subtasks. This is the reason why we decided to focus on orientation-prevailing tasks here, with predominant wrist motion control, and ignore reactionless positioning control. This

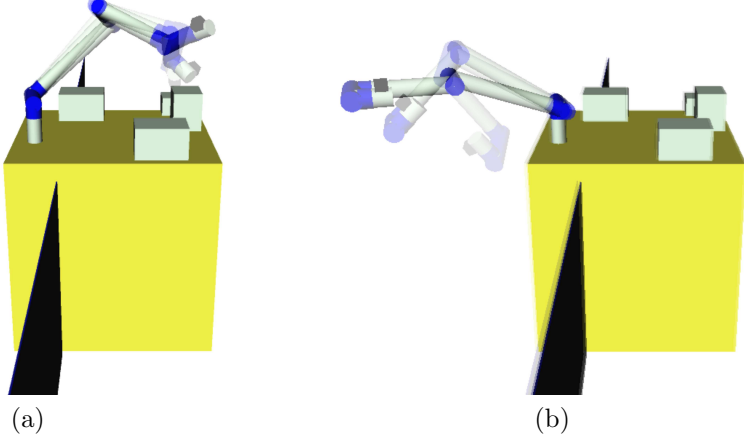


Figure 2: Reactionless motion of the manipulator model: (a) the predominant wrist motion and (b) elbow folding/unfolding motion. The dark areas signify solar panels.

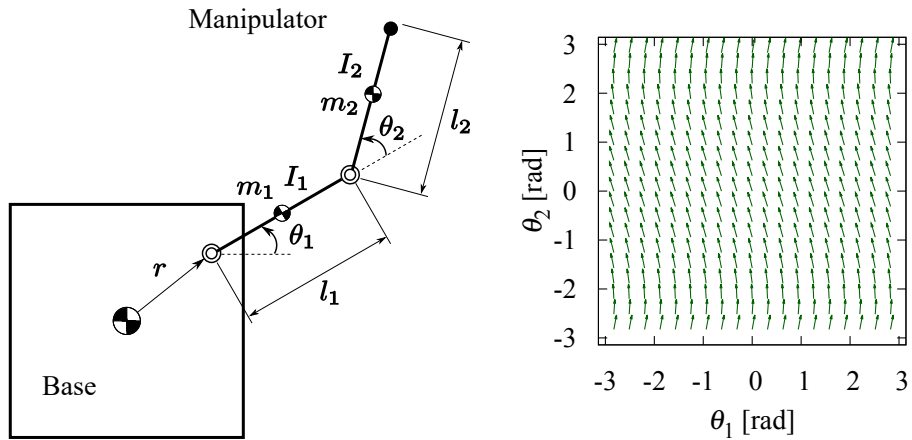


Figure 3: A planar two-DoF space manipulator model with $m_i = 100$ kg, $l_i = 1.0$ m ($i = 1, 2$); the base mass is $m_b = 1000$ kg. The vector field is obtained with $r = 0$ m.

approach distinguishes the present study from past ones which have focused exclusively on positioning tasks.

3.2. Reactionless motion vector field

The elbow folding/unfolding reactionless motion pattern identified in the previous section has been analyzed in past studies. One important aspect, however, has been left out of the discussion: the investigation of dynamic singularities under reactionless motion. Such singularities stem from rank deficiency of the coupling inertia matrix. Differently from kinematic singularities, dynamic singularities do not form static manifolds and are therefore very difficult to analyze. Here, we employ some tools from nonlinear system analysis to reveal the existence of fixed points and bifurcations, depending on the chosen manipulator attachment position. Fortunately, the elbow folding/unfolding reactionless motion pattern can be modeled with a planar two-DoF FFSR (cf. Fig. 3) which simplifies the analysis.

Reactionless motion with the two-DoF model can be generated by the following vector field:

$$\dot{\boldsymbol{\theta}} = b\mathbf{n}(\boldsymbol{\theta}) \quad (5)$$

where $\mathbf{n}(\boldsymbol{\theta}) \in \mathbb{R}^2$ is the only generic null-space vector in the kernel of the coupling inertia matrix, and b is an arbitrary scalar. Since the model is simple, $\mathbf{n}(\boldsymbol{\theta})$ can be obtained explicitly, e.g. via the co-factor method or singular value decomposition (SVD) of the coupling inertia matrix. Scalar b determines the intensity of the vector field at each configuration. Note that the

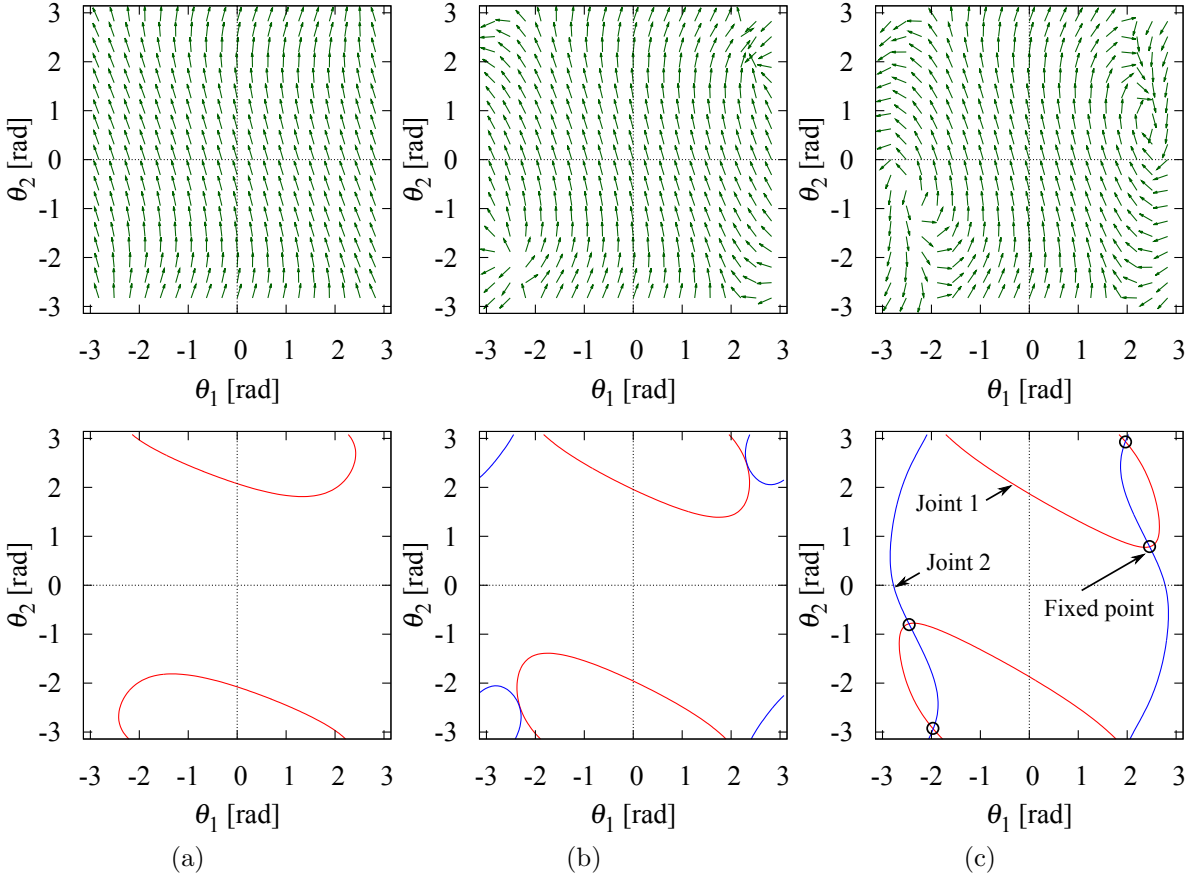


Figure 4: The vector field and nullclines for each joint direction when r variates as: (a) $r = 0.5$ m, (b) $r = 0.945$ m and (c) $r = 1.5$ m. The red and blue lines denote the nullclines for Joint 1 and 2, respectively.

reactionless property is determined by the direction of the vector field (i.e. by $\mathbf{n}(\theta)$), while field intensity b is related to the velocity magnitude only. Hence, for the purposes of analysis, (5) can be regarded as an autonomous nonlinear system. It is straightforward to show that at a fixed point, the coupling inertia matrix is rank deficient. Therefore, it would be desirable to avoid the appearance of fixed points.

Assume first that the manipulator is attached at the CoM of the base. This case is not realistic, but it is employed here for the sole purpose of comparative analysis. The mass and inertia moment of the base are $m_b = 1000$ kg, $I_b = 667$ kgm²; the length, mass and inertia moments of the links are $l_i = 1.0$ m, $m_i = 100$ kg and $I_i = 8.33$ kgm² ($i = 1, 2$), respectively. Note that the components of the coupling inertia matrix (and hence of the vector field) depend on the link-to-total-mass ratios: higher ratios induce larger base disturbances. Here we assumed a relatively high ratio of 1/12 for the purpose of analysis. In a real system, these ratios would be much smaller, as apparent from the data in Table 1. The resultant vector field is depicted in Fig. 3. First, note that the vector field does not depend on the rotation in Joint 1. Next, an important property becomes apparent: reactionless motion is predominantly composed of Joint 2 motion. The reason is that as reactionless motion conserves angular momentum at zero (or at a constant), motion in the joints that induce a large angular momentum cannot vibrate significantly. In our case, motion in Joint 1 induces a much larger moment than Joint 2. As a result, the above mentioned behavior is observed.

3.3. Fixed points and bifurcations

In the above example, it is seen that the system does not have any fixed points. It turns out, however, that the variation of the manipulator attachment position induces such points and moreover, bifurcations appear as well. Denote by r the distance between the attachment

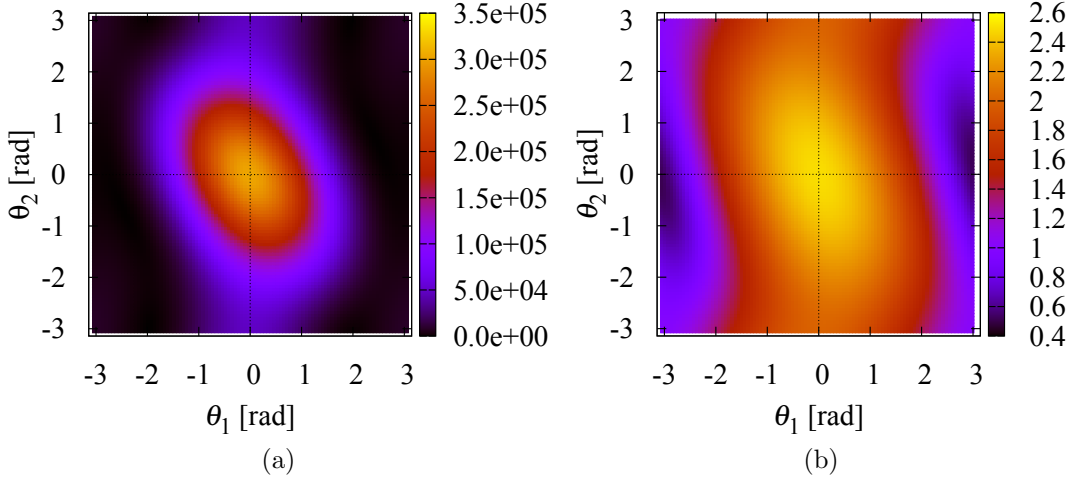


Figure 5: This figure shows (a) $\det(\tilde{\mathbf{M}}_{\omega m} \tilde{\mathbf{M}}_{\omega m}^T)$ and (b) the distance between the manipulator and the base CoMs as color maps.

position and the base CoM. This parameter plays an important role as a *bifurcation parameter*. Figure 4 depicts vector fields and nullclines for three representative values of r . The nullclines shown in red and blue in the lower part of the figure are for Joints 1 and 2, respectively. With a small value of r ($r = 0.5$ m), there are no fixed points: Joint 2 motion never stops. When r is increased ($r \approx 0.945$ m), two bifurcations appear. Further increase of r leads to the appearance of two fixed points at the intersections of the two nullclines. These fixed points then separate when the bifurcation parameter is increased to $r = 1.5$ m. Finally, when $r \rightarrow \infty$, two of the fixed points converge to $\theta_2 \rightarrow 0$ rad and the rest to $\theta_2 \rightarrow \pm\pi$ rad. These are the kinematic singularities of the respective fixed-base manipulator.

The result can be confirmed by the following rank deficiency analysis of the coupling inertia matrix. Note that whenever $\tilde{\mathbf{M}}_{\omega m}$ is rank deficient, $\det(\tilde{\mathbf{M}}_{\omega m} \tilde{\mathbf{M}}_{\omega m}^T) = 0$. The values of this determinant for $r = 1.5$ m are shown as a colored map in Fig. 5 (a). The determinant takes large values at the bright areas, while the most dark area represents the singularities. It is apparent that the determinant takes its maximum value at $\boldsymbol{\theta} = \mathbf{0}$. This is an extended-arm configuration s.t. the manipulator CoM is located farthest away from the base CoM. It turns out that $\det(\tilde{\mathbf{M}}_{\omega m} \tilde{\mathbf{M}}_{\omega m}^T)$ can be related to the distance between these two CoMs, as shown in Fig. 5 (b). Comparing the two plots in Fig. 5, it can be seen that the determinant takes large values whenever the distance is relatively large. Large CoM distance yields large moment of momentum and hence, large magnitude of the coupling angular momentum. Furthermore, note that there is no fixed point within the area where the distance is large. In the case of a spatial model, the directions of the joint axes also play an important role, in addition to the above qualitative characteristics.

4. Reactionless inspection task with a hand-held camera

In this section, we will introduce a practical task suitable for execution under reactionless motion control with a spatial redundant manipulator. First, the task description and the control law design will be addressed. Then, the performance of the proposed reactionless control approach will be compared to that of a conventional kinematic controller.

4.1. Task definition

One frequently appearing task for FFSR is inspection of devices mounted on the own satellite base or on the satellite to be serviced with a hand-held camera, as shown in Fig. 6. Such task was also performed within the ETS-VII mission [29] but without using reactionless control.

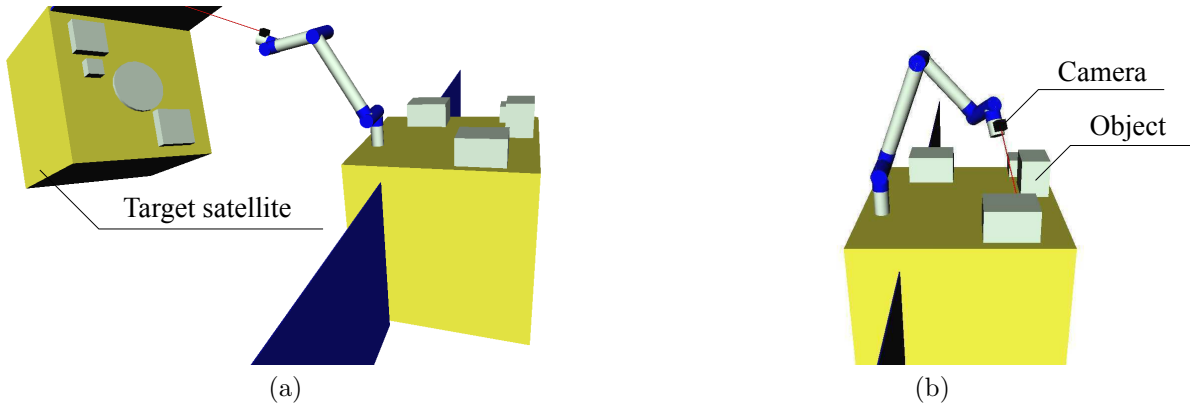


Figure 6: Inspection task using the hand-held camera to observe: (a) a target satellite to be refueled or captured and (b) the devices attached on the satellite base. The dark areas signify solar panels.

For camera inspection, once the arm is positioned appropriately, the camera view angle for inspection is changed by rotating the wrist. This task is expected to be performed multiple times during various missions such as construction, maintenance, debris removal and so on. Hence, this task is a good candidate for execution under reactionless motion control for improved work efficiency.

The following three control subtasks are considered necessary to accomplish the camera inspection task.

1. Reactionless constraint of the base attitude (three-DoF).
2. Orientation control of the wrist (three-DoF).
3. Stabilization of the wrist position.

The first control subtask ensures reactionless motion. The second one is essential for the camera inspection. The third control subtask is necessary to avoid a large deflection of the wrist from the initial position, since there is no position control subtask. The above subtasks will be simultaneously realized through consecutive null-space projections [30, 31], also known as the “task prioritization” approach [32]. Priorities are assigned among the tasks according to their relative importance. A higher-priority task can then be accomplished without being disturbed by the lower-priority tasks. This is ensured by projecting lower-priority tasks onto the common null-space of all higher-priority tasks.

4.2. Control law

The priorities are assigned as follows. The reactionless constraint is the highest-priority subtask, wrist orientation control is the second-priority and wrist position stabilization is the lowest-priority subtask. The control command for the joint velocity can then be obtained as follows:

$$\dot{\theta}^{ref} = {}^e\bar{J}_\omega^+ \omega_e^{ref} + k_g \mathbf{P}({}^w J_v^T) \Delta p_w \quad (6)$$

where $\omega_e \in \mathbb{R}^3$ is the angular velocity of the end-effector and ${}^e\bar{J}_\omega = [{}^e\mathbf{J}_\omega \mathbf{P}_{RNS}] \in \mathbb{R}^{3 \times 7}$ is the restricted Jacobian matrix [13] for the wrist subtask. Matrices ${}^e\mathbf{J}_\omega, {}^w\mathbf{J}_v \in \mathbb{R}^{3 \times 7}$ stand for the Jacobians w.r.t. the angular/linear velocity of the end-effector, respectively. The leading superscripts refer to the specific point associated with the velocities. The superscript for the end-effector, ${}^e(\circ)$, will be dropped henceforth to improve readability. $\mathbf{P} = \mathbf{P}_{RNS}(\mathbf{E} - \bar{J}_\omega^+ \bar{J}_\omega)$ is the combined null-space projector for the lowest-priority task. $\Delta p_w (= p_w - p_w^{init}) \in \mathbb{R}^3$ is the wrist deflection from the initial position, k_g is a positive gradient gain.

The structure of the control command is as follows. The first term is the end-effector orientation control projected onto the null-space of the coupling inertia matrix: this term can

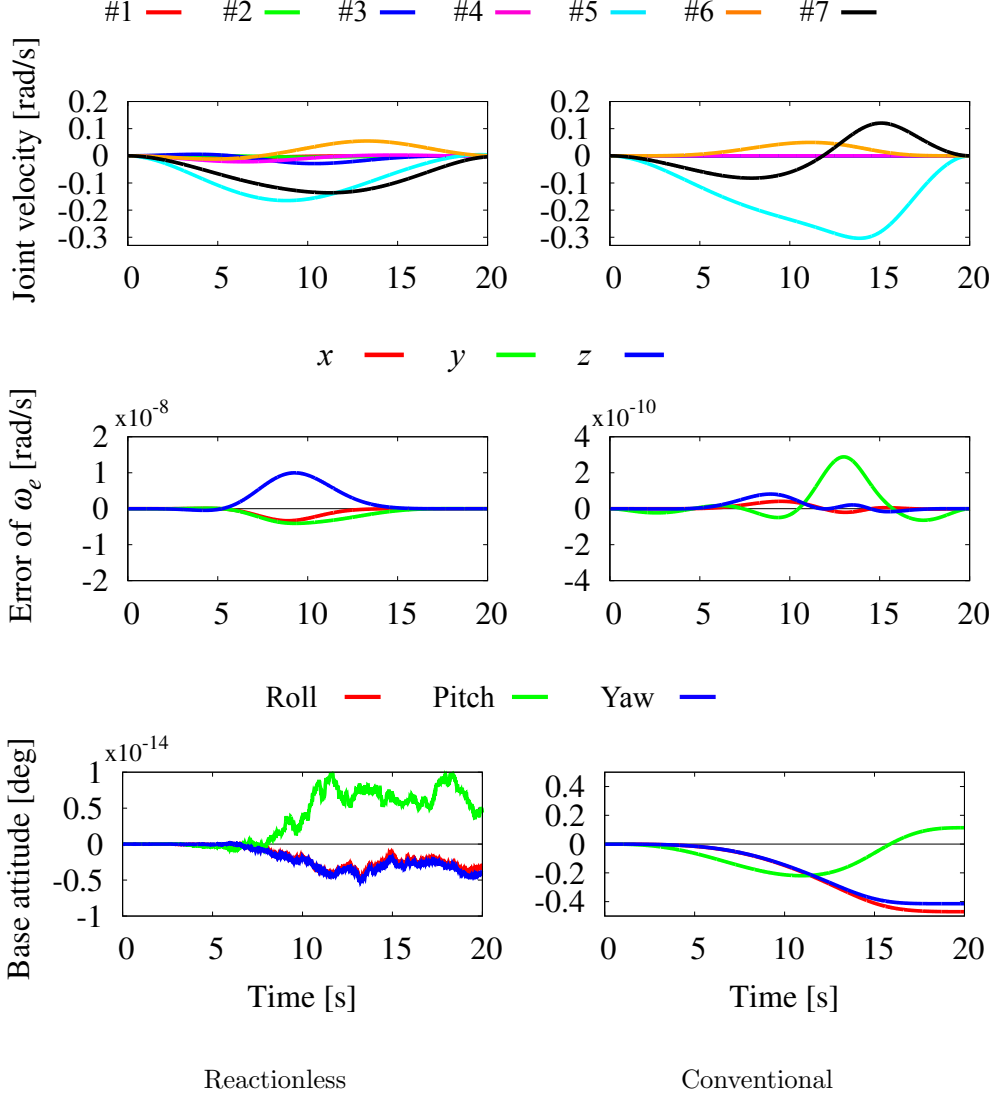


Figure 7: Simulation result from the satellite observation mission (Fig. 6 (a)). The result shows that the reactionless task can be accomplished, while a relatively large base attitude deviation is observed under the conventional control method. Note that, with exception of the joint velocity data graphs, different scales are employed.

accomplish the end-effector orientation control under the reactionless constraint. The second term minimizes the following potential function to stabilize the wrist position:

$$V = \frac{1}{2} \|\Delta \mathbf{p}_w\|^2. \quad (7)$$

This term does not disturb the higher priority tasks because it is projected onto the null-space of all higher priority tasks. It should be noted that $\bar{\mathbf{J}}_{\omega}^+$ may become rank-deficient. This is an algorithmic singularity which occurs when the end-effector and reactionless motion control subtasks are in conflict. The details of this singularity will be described below.

4.3. Numerical simulation

In what follows, we examine the performance under (6) by comparing it to that under a conventional inverse Jacobian controller that keeps the positioning subchain motionless. We assume the following two task scenarios for observing: (i) a satellite to be serviced (Fig. 6 (a)) and (ii) devices attached on the own satellite base (Fig. 6 (b)).

First, we verify the satellite observation case. The initial configuration is set as $[-90 -30 0 -70 180 -30 0]^T$ deg, as shown in Fig. 6 (a). The reference angular velocity is represented

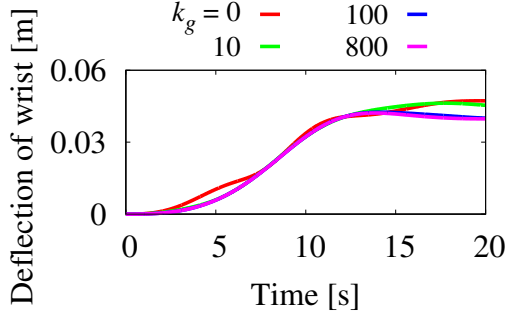


Figure 8: Wrist deflection during the satellite observation mission under reactionless motion with several gradient gains.

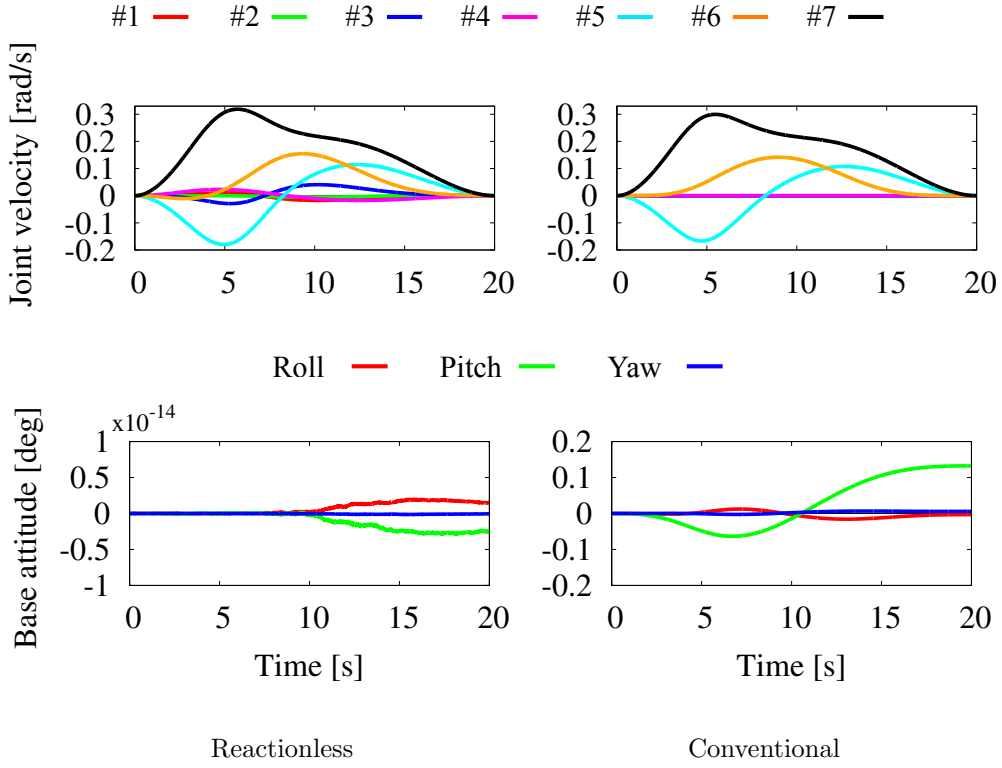


Figure 9: Simulation result from the inspection task of the FFSR surface mounted devices (Fig. 6 (b)).

in the inertial frame: $\omega_e^{ref} = \pi[s(t) \ 0 \ 0]^T$, where $0 \leq s(t) \leq 1$ denotes a fifth-order spline function. The simulation time and the gain are set at 20 s and $k_g = 100 \text{ kg/m} \cdot \text{s}$, respectively. The simulation results are displayed in Fig. 7. From the angular velocity error graphs it can be seen that the end-effector task is accomplished successfully in both simulations; there is only a subtle difference. This is not the case, though, for the base attitude deviation: under reactionless motion control the deviation is ignorable while under conventional control it is not². Also, this motion is realized with a relatively small displacement of the positioning subchain, as apparent from Fig. 8.

In the second scenario, we assume that the desired end-effector velocity is $\omega_e^{ref} = \pi[0 \ 0 \ -s(t)]^T \text{ rad/s}$, the initial configuration is set at $[90 \ -20 \ 180 \ 110 \ 0 \ 20 \ 0]^T \text{ deg}$ as shown in Fig. 6 (b). The other conditions are the same as in the previous simulation. The simulation results are shown in Fig. 9 and Fig. 10. First, it becomes apparent that in this case the base also remains undisturbed under reactionless motion while under conventional control, a

²The maximum allowable base attitude deviation for the ETS-VII mission was $\pm 0.05 \text{ deg}$.

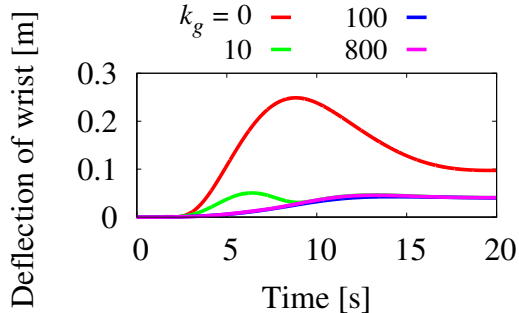


Figure 10: Wrist deflection during the inspection task of the FFSR surface mounted devices under reactionless motion with several gradient gains.

relatively large base attitude deviation is observed. Under reactionless motion, the effect of the cost function leads to a sufficiently small deviation from the initial wrist position as shown in Fig. 10.

To summarize, in both simulations of camera inspection, the efficacy of reactionless motion could be confirmed. In contrast, with the conventional controller a relatively large base attitude deviation was observed despite the prevailing use of the wrist subchain characterized by small mass and inertia moment components.

5. Singularities encountered during the reactionless inspection task

The following singularities could be encountered under the proposed control law:

- Kinematic singularities: $\det(\mathbf{J}_\omega \mathbf{J}_\omega^T) = 0$.
- Dynamic singularities (singularities of the coupling inertia matrix): $\det(\tilde{\mathbf{M}}_{\omega m} \tilde{\mathbf{M}}_{\omega m}^T) = 0$.
- Algorithmic singularities: $\det(\bar{\mathbf{J}}_\omega \bar{\mathbf{J}}_\omega^T) = 0$ with non-singular \mathbf{J}_ω and full row-rank $\tilde{\mathbf{M}}_{\omega m}$.

Kinematic singularities have been much discussed by various researchers, e.g. [33, 34]. The damped least-squares (DLS) method was introduced [35, 36] to deal with these type of singularity. The infinite growth of the joint velocity in the neighborhood of the singularity can be suppressed by a suitably defined damping factor. This method, however, has some drawbacks [37]: it causes workspace errors both in speed and motion direction. In addition, the determination of the damping factor is counter-intuitive. Another method, called the Singularity Consistent method, was proposed in [38]. Under this method, the manipulator can follow the desired path exactly, without causing a large joint velocity³.

In contrast, the second and third types of singularities have not been discussed extensively, so far. Fortunately, the singularities of the coupling inertia matrix do not pose a problem here because in the control law, only the null-space of the coupling inertia matrix appears. Indeed, in (6) the rank of restricted Jacobian $\bar{\mathbf{J}}_\omega$ depends on the conditioning of \mathbf{J}_ω only. This is because $\text{rank } \mathbf{P}_{RNS}$ grows when $\text{rank } \tilde{\mathbf{M}}_{\omega m}$ decreases. On the other hand, with regard to algorithmic singularities, we should first note that they need to be handled with care. Fortunately, such singularities seem to occur occasionally only. Nevertheless, in practice it is important to deal with this problem. Past studies have addressed this issue. In [39], for example, the algorithmic singularities of a planar six-DoF dual arm model were discussed. Another example is the

³The term “path” should be distinguished from “trajectory”: the former is characterized only geometrically while the latter includes time/velocity relations.

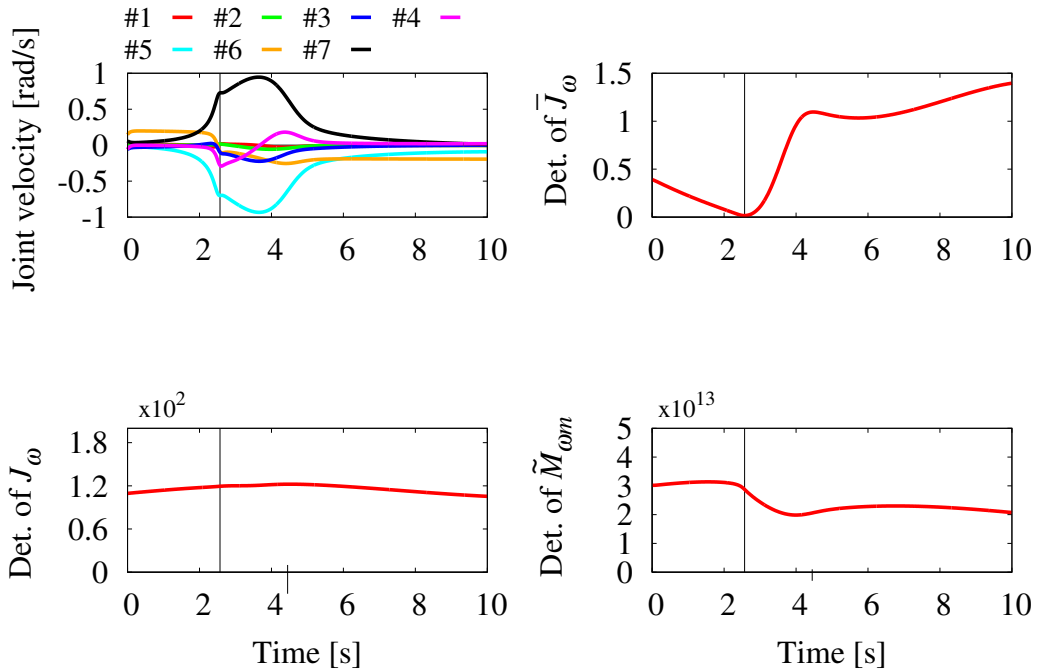


Figure 11: Encounter of an algorithmic singularity under the original control law.

singularity treatment technique proposed for reactionless motion control of flexible base robots [40]. However, these two methods cannot be applied in our case.

In what follows, two modifications of the control law will be presented to address the problem of algorithmic singularities. We encountered an algorithmic singularity under the following conditions. The initial configuration was the same as in the satellite observation task (cf. Fig. 6 (a)). The commanded angular velocity was however different: $\omega_e^{ref} = [0 \ -0.2 \ 0]^T$ rad/s. The simulation results are displayed in Fig. 11. In the graphs, the vertical line represents the time instant when the manipulator is passing near a singularity whereby $\det(\bar{J}_\omega \bar{J}_\omega^T)$ approaches zero but the other two determinants, $\det(J_\omega J_\omega^T)$ and $\det(\tilde{M}_{\omega m} \tilde{M}_{\omega m}^T)$, do not. Hence, this singularity can be recognized as an algorithmic one. From the joint velocity graphs it is seen that near the singularity, Joints 5 and 7 rotate in opposite directions with high joint rates. This type of behavior is observed at singularities of the Euler angles [41] as well as at wrist singularities [42].

In what follows, we examine the capability of two known singularity treatment methods to handle the algorithmic singularity thus observed.

5.1. Singularity treatment with the Damped Least-Squares inverse

Originally, the DLS generalized inverse is obtained by adding damping factors to the singular values appearing as denominators in the SVD, to suppress high joint rates. This method, however, introduces significant errors. The problem can be alleviated with a modification of the DLS generalized inverse that is obtained through a so-called numerical filtering technique [43]. Accordingly, the generalized inverse of \bar{J}_ω is obtained in the following form:

$$\bar{J}_\omega^\# = \bar{J}_\omega^T \left(\bar{J}_\omega \bar{J}_\omega^T + \lambda^2 \mathbf{u}_3 \mathbf{u}_3^T \right)^{-1} \quad (8)$$

where λ is a damping factor, $\mathbf{u}_3 \in \mathbb{R}^3$ is the left singular vector associated with the minimum singular value σ_3 , $(\circ)^\#$ represents the DLS inverse. This matrix replaces the pseudoinverse in the original control law, (6).

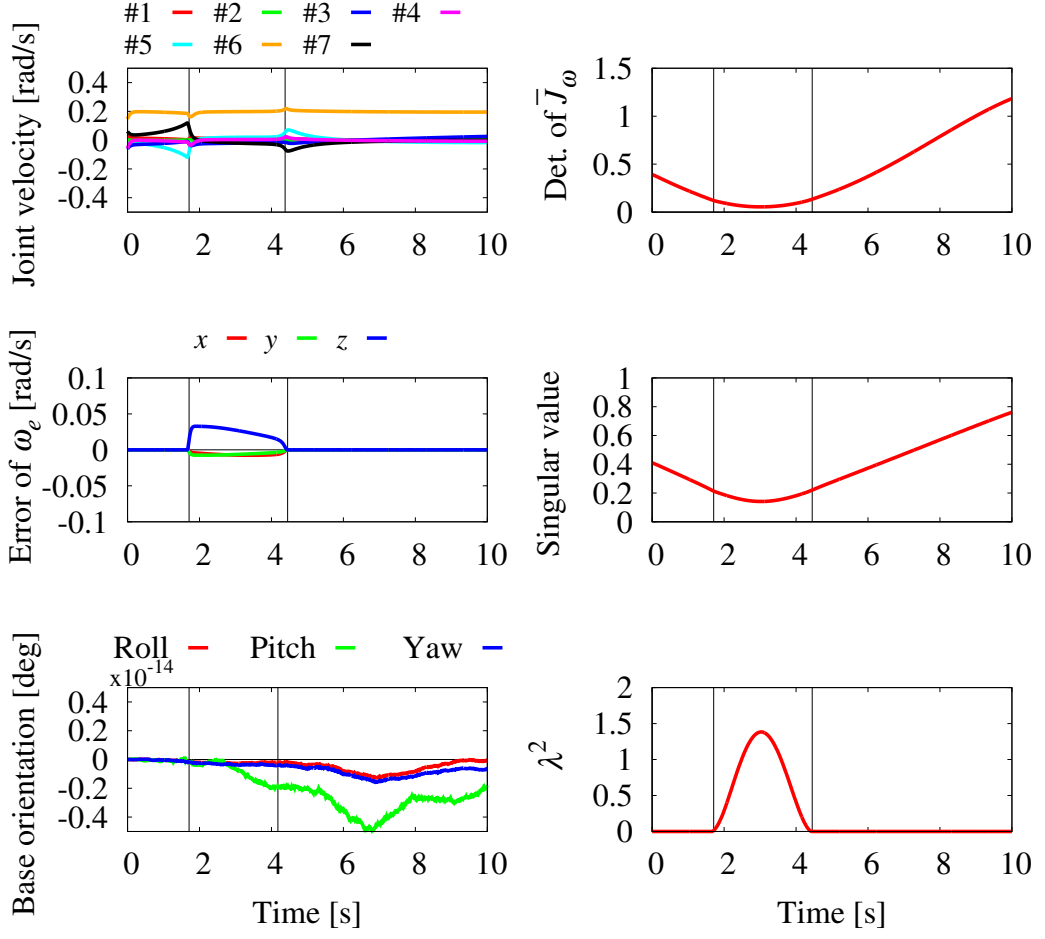


Figure 12: Reactionless camera inspection task performed in the neighborhood of an algorithmic singularity under DLS-modified control law. Excessive joint velocity within the singular region (marked by the vertical lines) is suppressed.

Further on, to determine damping factor λ , we resume to the SVD of $\bar{\mathbf{J}}_\omega$. DLS inverse (8) is then rewritten as:

$$\bar{\mathbf{J}}_\omega^\# = \sum_{i=1}^2 \frac{1}{\sigma_i} \mathbf{v}_i \mathbf{u}_i^T + \frac{\sigma_3}{\sigma_3^2 + \lambda^2} \mathbf{v}_3 \mathbf{u}_3^T \quad (9)$$

where $\sigma_1 \geq \sigma_2 \geq \sigma_3$ are the singular values and $\mathbf{u}_i \in \mathbb{R}^3$, $\mathbf{v}_i \in \mathbb{R}^7$ are the associated left and right singular vectors. It can be seen that the DLS inverse (8) is characterized by a damping factor appearing only in the last term, containing the minimum singular value. Therefore, when compared with the original DLS inverse that adds damping into all terms, the error of the solution can be reduced. Then, based on [44], the damping factor is obtained as follows:

$$\lambda^2 = \begin{cases} 0 & \varepsilon < \sigma_3 \\ (1 - \frac{2\sigma_3^2}{\varepsilon^2} + \frac{\sigma_3^4}{\varepsilon^4}) \lambda_{max}^2 & \sigma_3 \leq \varepsilon \end{cases} \quad (10)$$

where ε defines the singular region, which has to be introduced to define the neighborhood of the singularity. Scalar λ_{max} determines the maximum value of the damping factor. Note that, to obtain a smooth transition at the border of the singular region, we had to modify the original expression in [44] by adding the σ_3^4/ε^4 term.

The performance of the DLS inverse for this controller is verified via numerical simulations. The simulation conditions are the same as above. The singular region is defined by $\varepsilon = 0.2$

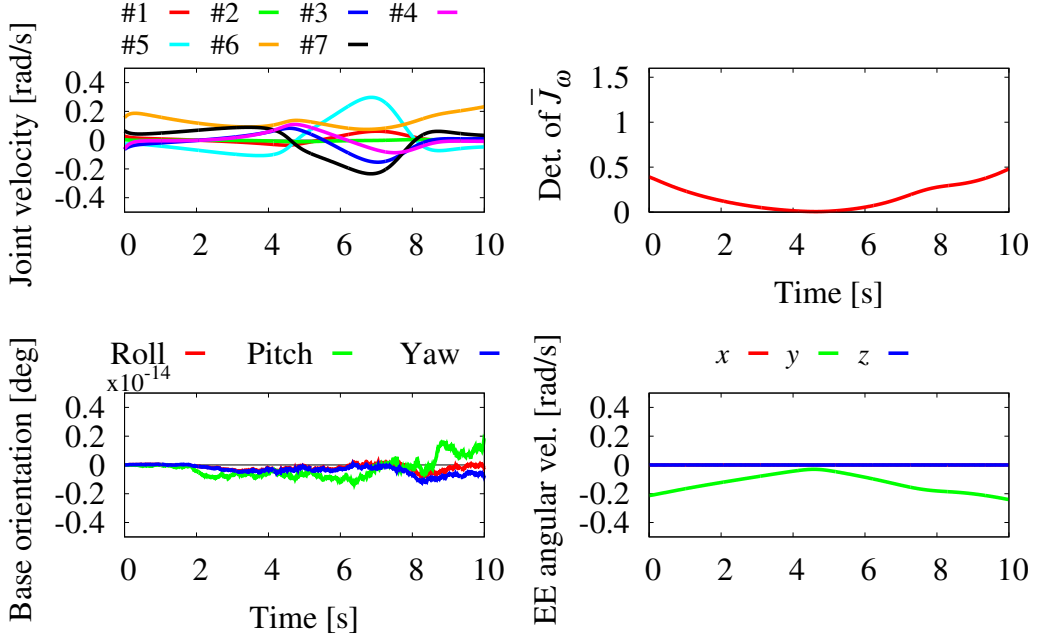


Figure 13: Reactionless camera inspection task performed in the neighborhood of an algorithmic singularity under SC control law (13). Within neighborhood $\det(\bar{\mathbf{J}}_\omega \bar{\mathbf{J}}_\omega^T) \approx 0$, end-effector (EE) angular velocity decreases but no excessive joint velocity is observed.

and the maximum damping value set at $\lambda_{max}^2 = 2$. The results are displayed in Fig. 12. In the graphs, the singular region is indicated by the two vertical lines ($1.71 \text{ s} \leq t \leq 4.18 \text{ s}$). From the results it is apparent that the growth of the joint velocity has been successfully suppressed through the damping factor. However, an end-effector angular velocity tracking error can be observed within the singular region. This is caused by the damping factor, as already explained. On the other hand, the base attitude does not deviate, even within the singular region.

5.2. The Singularity Consistent method [45]

We will examine the possibility to make use of the Singularity Consistent (SC) method for singularity treatment. It was clarified that the DLS method introduces an error in the direction of the velocity command since the singular direction, i.e. \mathbf{v}_3 , has to be avoided. In contrast, the SC method actively makes use of this direction and therefore, the manipulator can follow the direction of the commanded end-effector velocity, correctly. An error only appears in the speed along the path. If we consider a teleoperation task, such an error is not problematic because the operator can modify the desired end-effector speed according to the task conditions [46, 47].

We will make use of natural motion [48, 49], i.e. end-effector motion with velocity in proportion to the determinant of the Jacobian matrix. This motion is obtained with a constant vector field magnitude (a constant b). There is no need to define a singular region then, and hence, to switch the control input, as with the DLS method. According to the SC method, the inverse of $\bar{\mathbf{J}}_\omega$ can be obtained as follows:

$$\bar{\mathbf{J}}_\omega^+ = b \sum_{i=1}^3 \mu_i \mathbf{v}_i \mathbf{u}_i^T \quad (11)$$

$$\mu_i = \prod_{j=1, j \neq i}^3 \sigma_j \quad (12)$$

From (12), we can see that μ_1 and μ_2 become small near the singularity, because their values are

proportional to the minimum singular value that approaches 0 in the vicinity of the singularity. Hence, the \mathbf{v}_3 related term is actively used.

We verify the performance of this method through numerical simulations. The simulation conditions are the same as in the DLS case. Empirically, the constant scalar was set at $b = 1.7$. In addition, to avoid a large joint velocity obtained from the null-space term, we multiply the term by $\det(\bar{\mathbf{J}}_\omega \bar{\mathbf{J}}_\omega^T)$ as follows:

$$\dot{\boldsymbol{\theta}}^{ref} = \bar{\mathbf{J}}_\omega^+ \boldsymbol{\omega}_e^{ref} + k_g \det(\bar{\mathbf{J}}_\omega \bar{\mathbf{J}}_\omega^T) \mathbf{P}({}^w \mathbf{J}_v^T) \Delta \mathbf{p}_w \quad (13)$$

The simulation results are displayed in Fig. 13. The results show that the rapid change of joint velocity can be avoided. In addition, it is seen that the end-effector follows the commanded velocity direction y , which is in contrast with the result from the DLS simulation. The effect of the method is only upon the speed, which decreases in the vicinity of the singularity.

6. Kinetic energy based analysis under zero base-attitude deviation

So far, we have clarified that there are two possibilities to perform a manipulator task with a FFSR: the conventional approach based on the inverse Jacobian and the proposed reactionless approach. In the former case, base attitude deviation due to manipulator motion reaction is compensated for by the satellite attitude control system (ACS), while in the latter case there is no need to use the ACS for this purpose. As mentioned in the Introduction, previous research has identified longer execution time of the manipulator task as a disadvantage of the conventional method: the manipulator has to be driven at lower speed to avoid large base disturbance and hence, saturation of the ACS. It would also be interesting to examine and compare the kinetic energy flow with this two approaches. Although not directly related to power consumption, the kinetic energy distribution picture may provide important insights, as will be shown in what follows.

First, we identify the minimum energy motion under zero base-attitude deviation ($\boldsymbol{\omega}_b \approx \mathbf{0}$) and show that it is almost identical with reactionless motion control. The intuitive reason behind this is that under reactionless motion control, there is no need to use the reaction wheels. In contrast, under conventional control, the reaction wheels may need to frequently accelerate/decelerate to compensate a significantly varying reaction stemming from the manipulator motion.

6.1. Kinetic energy representation in terms of joint velocity

The equation of motion of the system with reaction wheels can be represented from [22] as:

$$\begin{bmatrix} \tilde{\mathbf{M}}_\omega & \tilde{\mathbf{M}}_{\omega m} & \tilde{\mathbf{M}}_{\omega r} \\ \tilde{\mathbf{M}}_{\omega m}^T & \tilde{\mathbf{M}}_m & \mathbf{0} \\ \tilde{\mathbf{M}}_{\omega r}^T & \mathbf{0} & \tilde{\mathbf{M}}_r \end{bmatrix} \begin{bmatrix} \boldsymbol{\omega}_b \\ \ddot{\boldsymbol{\theta}} \\ \ddot{\boldsymbol{\phi}} \end{bmatrix} + \begin{bmatrix} \mathbf{c}_b \\ \mathbf{c}_m \\ \mathbf{c}_r \end{bmatrix} = \begin{bmatrix} \mathbf{0} \\ \boldsymbol{\tau}_m \\ \boldsymbol{\tau}_r \end{bmatrix} \quad (14)$$

where the $\mathbf{c}_{(o)}$ terms denote nonlinear Coriolis and centrifugal forces, $\boldsymbol{\tau}_m$ and $\boldsymbol{\tau}_r$ are manipulator joint and reaction wheel torque vectors. $\tilde{\mathbf{M}}_m$ is obtained from manipulator link inertia matrix⁴

$$\mathbf{M}_m = \sum_{i=1}^n \left\{ m_i \mathbf{J}_{vi}^T \mathbf{J}_{vi} + \mathbf{J}_{\omega i}^T \mathbf{I}_i \mathbf{J}_{\omega i} \right\}. \quad (15)$$

$m_i, \mathbf{I}_i \in \mathbb{R}^3$ are the i -th link's mass and inertia tensor, $\mathbf{J}_{vi}, \mathbf{J}_{\omega i} \in \mathbb{R}^{3 \times n}$ stand for the Jacobians w.r.t. link CoM linear and angular velocities, respectively. Similar to the notation used in

⁴Known from introductory texts on manipulator dynamics.

(2), the “tilde” signifies a modification applied to account for the elimination of the satellite base velocity from the equation of motion. Note that the integral of (14) yields momentum conservation equation (2).

For the comparative analysis, it is convenient to represent the kinetic energy in terms of joint velocity. The kinetic energy related to the above equation of motion is:

$$T = \frac{1}{2} \boldsymbol{\omega}_b^T \tilde{\mathbf{M}}_\omega \boldsymbol{\omega}_b + \boldsymbol{\omega}_b^T [\tilde{\mathbf{M}}_{\omega m} \quad \tilde{\mathbf{M}}_{\omega r}] \begin{bmatrix} \dot{\boldsymbol{\theta}} \\ \dot{\boldsymbol{\phi}} \end{bmatrix} + \frac{1}{2} [\dot{\boldsymbol{\theta}}^T \quad \dot{\boldsymbol{\phi}}^T] \begin{bmatrix} \tilde{\mathbf{M}}_m & \mathbf{0} \\ \mathbf{0} & \tilde{\mathbf{M}}_r \end{bmatrix} \begin{bmatrix} \dot{\boldsymbol{\theta}} \\ \dot{\boldsymbol{\phi}} \end{bmatrix}. \quad (16)$$

The first term on the r.h.s. represents the partial kinetic energy stemming from base rotation, the second term is the coupling kinetic energy between the base and the manipulator or the reaction wheels. Finally, the third term is the partial kinetic energy produced by the manipulator and the reaction wheels. Next, assuming zero base attitude deviation, the above expression simplifies as:

$$T = \frac{1}{2} \dot{\boldsymbol{\theta}}^T \tilde{\mathbf{M}}_m \dot{\boldsymbol{\theta}} + \frac{1}{2} \dot{\boldsymbol{\phi}}^T \tilde{\mathbf{M}}_r \dot{\boldsymbol{\phi}}. \quad (17)$$

Further on, from angular momentum conservation equation (2), the reaction wheel speed can be represented as a function of the joint velocity, $\dot{\boldsymbol{\phi}} = -\tilde{\mathbf{M}}_{\omega r}^{-1} \tilde{\mathbf{M}}_{\omega m} \dot{\boldsymbol{\theta}}$. Substitute this expression into (17) to obtain the kinetic energy as a function of the joint velocity:

$$\begin{aligned} T &= \frac{1}{2} \dot{\boldsymbol{\theta}}^T \left(\tilde{\mathbf{M}}_m + \tilde{\mathbf{M}}_{\omega m}^T (\tilde{\mathbf{M}}_{\omega r} \tilde{\mathbf{M}}_r^{-1} \tilde{\mathbf{M}}_{\omega r}^T)^{-1} \tilde{\mathbf{M}}_{\omega m} \right) \dot{\boldsymbol{\theta}} \\ &= \frac{1}{2} \dot{\boldsymbol{\theta}}^T \left(\tilde{\mathbf{M}}_m + I_r^{-1} \tilde{\mathbf{M}}_{\omega m}^T \tilde{\mathbf{M}}_{\omega m} \right) \dot{\boldsymbol{\theta}} \\ &= \frac{1}{2} \dot{\boldsymbol{\theta}}^T \hat{\mathbf{M}} \dot{\boldsymbol{\theta}}. \end{aligned} \quad (18)$$

$\hat{\mathbf{M}} = \hat{\mathbf{M}}_m + \hat{\mathbf{M}}_r$ is the inertia matrix of the manipulator under zero attitude deviation. Matrices $\hat{\mathbf{M}}_m = \tilde{\mathbf{M}}_m$ and $\hat{\mathbf{M}}_r = I_r^{-1} \tilde{\mathbf{M}}_{\omega m}^T \tilde{\mathbf{M}}_{\omega m} \in \mathbb{R}^{n \times n}$ are inertias associated with the manipulator and the reaction wheels, respectively. In the above derivation, we have assumed that the ACS comprises three reaction wheels mounted on mutually orthogonal axes, such that $\tilde{\mathbf{M}}_r = \text{diag}(I_r, I_r, I_r)$. Also, we assumed that $\tilde{\mathbf{M}}_{\omega r} \approx \tilde{\mathbf{M}}_r$, which is justified by relation $\tilde{\mathbf{M}}_{\omega r}^T \boldsymbol{\omega}_b = -\tilde{\mathbf{M}}_r \dot{\boldsymbol{\phi}}$ obtained from the integral of (14), and the orthogonal arrangement of the reaction wheels, yielding $\boldsymbol{\omega}_b \approx \dot{\boldsymbol{\phi}}$.

The direction of instantaneous minimum energy motion in joint space can be obtained through SVD of matrix $\hat{\mathbf{M}}$ [50]. Note that the meaning of each singular vector can be interpreted as normalized joint velocity, while the respective singular value signifies the instantaneous kinetic energy induced by that velocity. It should be then apparent that the lowest singular value will represent the instantaneous minimum kinetic energy, while the respective singular vector will determine the instantaneous minimum energy motion direction.

6.2. Relation between reactionless motion and instantaneous minimum energy motion

Here, we compare reactionless motion and the instantaneous minimum energy motion via numerical analysis. For the sake of simplicity, we focus on models comprising only one-DoF reactionless motion.

6.2.1. Two-DoF planar manipulator

First, the kinetic energy pertinent to the two-DoF planar model shown in Fig. 3 is examined. The link lengths, masses and inertia moments are set at $l_i = 1.0$ m, $m_i = 100$ kg and $I_i = 8.3$ kgm² ($i = 1, 2$), respectively. The reaction wheel’s mass and inertia moment are set at $m_r = 10$ kg, $I_r = 0.11$ kgm². The manipulator attachment position is defined as $r = 0.945$ m.

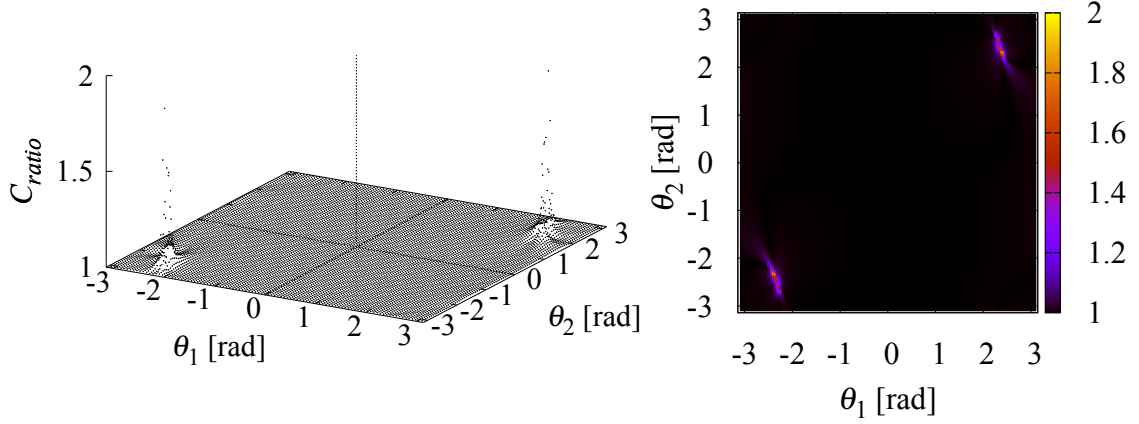


Figure 14: The distribution of the cost function with the two-DoF model.

The following cost function will be used to evaluate the energy relation for reactionless and instantaneous minimum energy motion:

$$C_{ratio} = \frac{T_{RNS}}{T_{min}}. \quad (19)$$

T_{RNS} and T_{min} denote the kinetic energies under reactionless and instantaneous minimum energy motion, respectively. T_{min} is calculated as explained in the previous section. T_{RNS} is obtained in the same way, as the minimum singular value of coupling inertia matrix $\tilde{\mathbf{M}}_{\omega m}$. Further on, because $T_{RNS} \geq T_{min}$ at all configurations, $C_{ratio} \geq 1$ is ensured. This function will be calculated at a mesh of 10K points in joint space, with $-\pi \leq \theta_i \leq \pi$, ($i = 1, 2$). For each coordinate, the joint angles are discretized with $\Delta\theta_i = 6.28 \times 10^{-2}$ rad.

The distribution of C_{ratio} is displayed in Fig. 14. From the result, we can confirm that $C_{ratio} \approx 1$ at almost all points. Indeed, the average of C_{ratio} is 1.002 among all points. Hence, reactionless and instantaneous minimum energy motion are equivalent for this model. It should be noted though that there are large discrepancies at specific points. This issue will be discussed below.

6.2.2. Four-DoF spatial manipulator

Next, the positioning subchain of the seven-DoF redundant manipulator introduced in Section 3 will be used to evaluate the energy ratio. The reaction wheel parameters are the same as in the planar case. The same cost function is also used to evaluate the equivalence. The calculation range is as follows:

$$\begin{aligned} -\pi &\leq \theta_i \leq \pi \\ \Delta\theta_i &= 0.125 \text{ rad } (i = 1, 3, 4) \end{aligned} \quad (20)$$

$$\begin{aligned} -\frac{\pi}{2} &\leq \theta_2 \leq \frac{\pi}{2} \\ \Delta\theta_2 &= 0.0628 \text{ rad} \end{aligned} \quad (21)$$

where we restrict the range of Joint 2 because almost all configurations outside the above range have no meaning since they would impose a collision with the satellite. The cost function is calculated at 6.25×10^6 points. Since the number of parameters is large, we parameterize the distribution of C_{ratio} by Joint 1 and 2. In Fig. 15 (a) and (b) two distribution maps are shown obtained through parametrization $(\theta_1, \theta_2) = (-3.05, 0.403)$ rad and $(\theta_1, \theta_2) = (-\pi, 0)$ rad, respectively. Apparently, except for few configurations, reactionless motion is very close to minimum-energy motion, as in the planar case. Even in the worse case shown in Fig. 15 (b), the average value of C_{ratio} is 1.14, which is sufficiently close to one. The high values of C_{ratio}

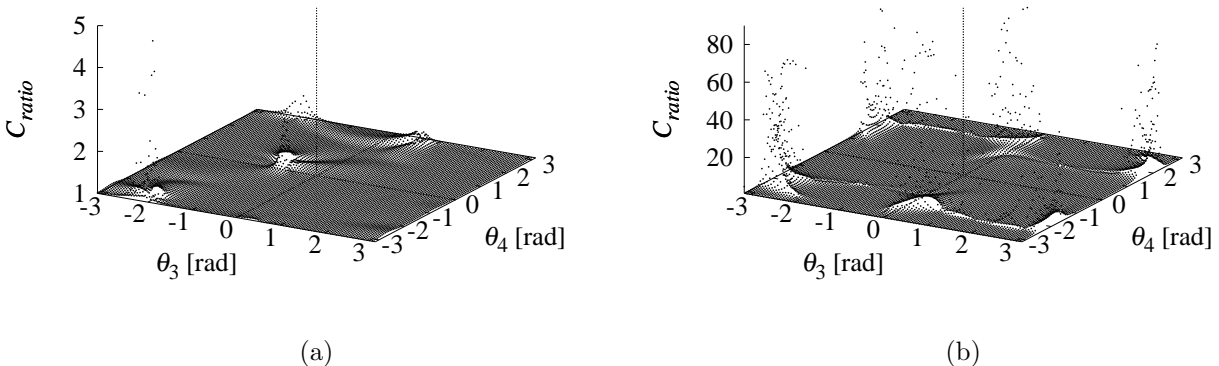


Figure 15: The disistribution of cost function with the four-DoF spatial manipulator model: (a) regularly appearing distribution $(\theta_1, \theta_2) = (-3.05, 0.403)$ rad and (b) near the singularity $(\theta_1, \theta_2) = (-\pi, 0)$ rad.

observed at specific points appear in the vicinity of the singularities of the coupling inertia matrix. This also becomes apparent when comparing Fig. 14 with Fig. 4 (b).

As a result of this brief analysis, we can conclude that reactionless motion approximates fairly well minimum-energy motion. In other words, under minimum-energy control the usage of the reaction wheels would be avoided to a great extent.

6.3. Comparative study for the camera inspection task

The aim is to evaluate the performance of reactionless motion control and conventional control plus reaction wheel compensation in terms of kinetic energy. To this end, we introduce the following cost functions (energies):

$$C_{max} = \frac{1}{2} \max_{t_0 \leq t \leq t_f} \left(\dot{\theta}^T(t) \hat{M} \dot{\theta}(t) \right) \quad (22)$$

$$C_{sum} = \frac{1}{2} \int_{t_0}^{t_f} \dot{\theta}^T(t) \hat{M} \dot{\theta}(t) dt. \quad (23)$$

In order to realize zero base-attitude deviation with the reaction wheels, the reaction wheel torque should be:

$$\tau_r^{ref} = -\frac{d}{dt}(\tilde{M}_{\omega m}\dot{\theta}^{ref}(t)) \quad (24)$$

where $\dot{\theta}^{ref}$ is the pre-defined reference control command for the manipulator. We compare the above costs obtained during the camera inspection task. The conventional controller is the inverse Jacobian controller for the wrist assembly, as already introduced in the previous sections.

We first present detailed data for one simulation. The conditions are the same as those used in Section 4 (the case of Fig. 6 (a)): the initial configuration is set at $[-90 \ -30 \ 0 \ -70 \ 180 \ -30 \ 0]^T$ deg, the reference angular velocity is $\omega_e^{ref} = \pi[s(t) \ 0 \ 0]^T$, where $0 \leq s(t) \leq 1$ denotes a fifth-order spline function; the simulation time and the gain are set at 20 s and $k_g = 100$ kg/(m · s), respectively. The results are displayed in Fig. 16. We can see that the kinetic energy produced by the reaction wheels is quite larger than that by the manipulator. Hence, in this case, we can confirm that reactionless motion control has an advantage in terms of energy consumption, as described above. In addition, there would also be an advantage in terms of task execution time: if this inspection task is to be performed under conventional

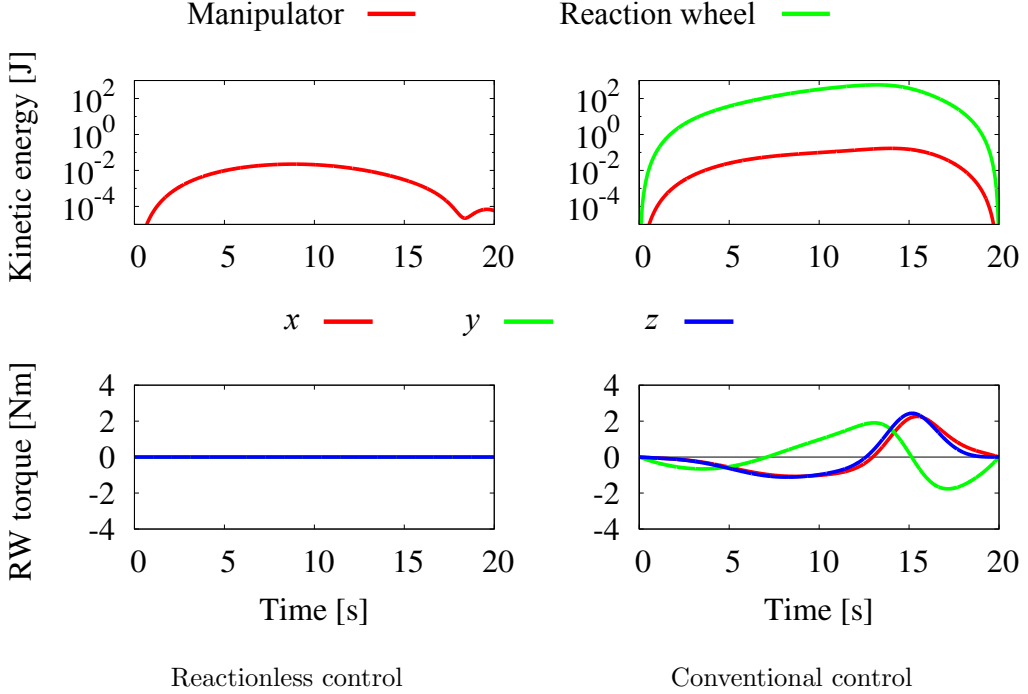


Figure 16: Comparison of the instantaneous kinetic energies in the cases of reactionless and conventional (plus reaction wheels) control.

control plus reaction wheel compensation, the manipulator would have to be driven at lower speed because the limitation of the reaction wheel torque is in general quite low⁵.

Next, we compare the cost for five different initial configurations and desired motion chosen at random. In all cases, the simulation time is set at 20 s. The results are displayed in Fig. 17. The red bar expresses the results under reactionless motion control; the green bar shows the results under conventional control plus reaction wheels used. Note that the vertical axis represents the cost in logarithmic scale. From the results it can be seen that the kinetic energy under reactionless motion is quite smaller (about one thousand times smaller) than that under conventional control plus reaction wheels.

To understand the above results, we should identify specific properties of the kinetic energies produced by the manipulator and the reaction wheels under zero base-attitude deviation. Consider a general n -link manipulator model. Referring to (15), matrix $\hat{\mathbf{M}}_r$ can be expressed as follows:

$$\begin{aligned}\hat{\mathbf{M}}_r &= \frac{1}{I_r} \tilde{\mathbf{M}}_{\omega m}^T \tilde{\mathbf{M}}_{\omega m} \\ &= \frac{1}{I_r} \sum_{i=1}^n \left(m_i^2 \mathbf{J}_{vi}^T \mathbf{r}_i^{\times T} \mathbf{r}_i^{\times} \mathbf{J}_{vi} + \mathbf{J}_{\omega i}^T \mathbf{I}_i \mathbf{I}_i \mathbf{J}_{\omega i} + m_i \mathbf{J}_{\omega i}^T \mathbf{I}_i \mathbf{r}_i^{\times} \mathbf{J}_{vi} + [\mathbf{m}_i \mathbf{J}_{\omega i}^T \mathbf{I}_i \mathbf{r}_i^{\times} \mathbf{J}_{vi}]^T \right)\end{aligned}\quad (25)$$

where $\mathbf{r}_i \in \mathbb{R}^3$ is the position vector of the i -th link CoM w.r.t. the base CoM. Note that terms related to base translation are ignored for the sake of simplicity. From (15), it can be seen that the kinetic energy induced by the manipulator motion is represented as a linear function in terms of the inertia parameters of the manipulator. On the other hand, from (25) it becomes apparent that the reaction wheel related energy is a quadratic function of these parameters; it is also in proportion to the inverse of the inertia moment of the reaction wheel, which is usually much smaller than one. Hence, we can conclude that the kinetic energy produced by the reaction wheels, when expressed in terms of joint velocity, is much larger than that

⁵For instance, in the ETS-VII experiment it was 0.1 Nm.

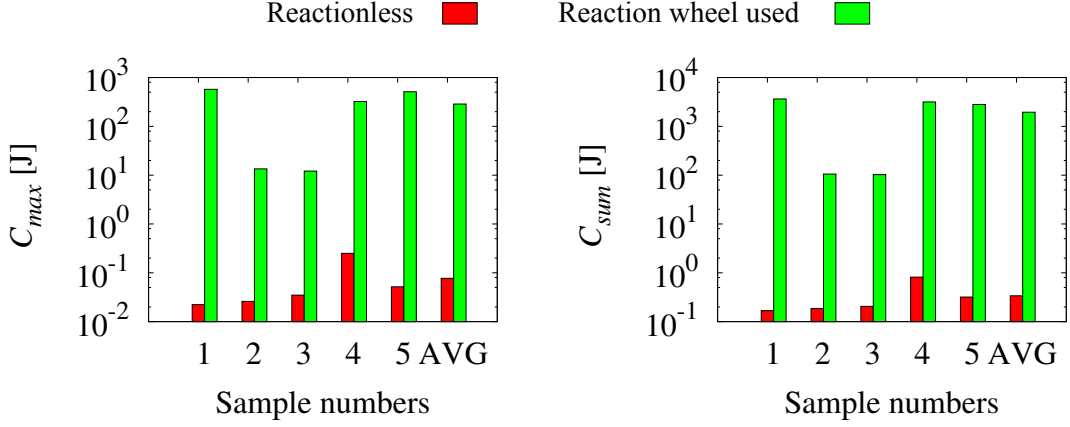


Figure 17: Comparison of energy functions C_{max} and C_{sum} under five randomly chosen conditions.

produced by the manipulator itself. This feature would make reactionless motion potentially more effective than the conventional approach relying on the usage of reaction wheels.

The result from the above comparative analysis stems from the large kinetic energy pertinent to the reaction wheels, as explained with (25). Apparently, the mass/inertia of the base is quite large and therefore, the compensation of base rotation induced by the manipulator reactions requires heavy involvement of the reaction wheels. In case of reactionless motion, such involvement is completely unnecessary.

7. Conclusions

In this work, we have shown that inspection tasks with a hand-held camera can be performed by a FFSR under reactionless motion. The conditions used to assess the performance via simulations were selected to be close to reality: we used a three-dimensional model, with a “common” manipulator arm of seven DoFs and mass/inertia parameters borrowed from the ETS-VII mission. The manipulator attachment position was also decided based on that mission. We have shown that the distance between the position and the CoM of the satellite base can be related to the singularities of the coupling inertia matrix (dynamic singularities). With the proposed control law, the effect of these singularities is ignorable though. More important are algorithmic singularities, which we tackled successfully with singularity treatment techniques developed for terrestrial manipulators.

Further on, we have shown that the implementation of reactionless motion generation and control requires careful task and kinematic structure dependent analysis. For the chosen task, it was shown that the set of reactionless motions is represented approximately as a superposition of predominant wrist and elbow motions. Using predominant wrist motion, we designed a task-of-priority controller for the inspection task. The base attitude (reactionless) constraint was considered as the primary task; the end-effector orientation control was the secondary one; wrist position stabilization was performed as the third-priority subtask. Via numerical simulations, it was shown that this reactionless task yields better results when compared with the traditional inverse Jacobian controller.

We performed also a comparative analysis in terms of kinetic energy between reactionless and conventional (plus reaction wheels) control. It turns out that, when expressed in terms of manipulator joint velocity, the kinetic energy of the reaction wheels becomes a quadratic function of the dynamic parameters of the manipulator, while the kinetic energy of the manipulator is a linear one. This feature renders reactionless motion effective in terms of kinetic energy.

Acknowledgements

The authors appreciate the help provided by Kengo Tamoto with some of the simulations and figures. We thank the anonymous reviewers for their constructive comments, which helped us to improve the manuscript.

References

- [1] Z. Vafa, S. Dubowsky, On the dynamics of manipulators in space using the virtual manipulator approach, in: Proceedings of IEEE International Conference on Robotics and Automation, 1987, pp. 579–585.
- [2] A. Flores-Abad, O. Ma, K. Pham, S. Ulrich, A review of space robotics technologies for on-orbit servicing, *Progress in Aerospace Sciences* 68 (2014) 1–26.
- [3] Y. Masutani, F. Miyazaki, S. Arimoto, Sensory feedback control for space manipulators, in: Proceedings of IEEE International Conference on Robotics and Automation, 1989, pp. 1346–1351.
- [4] Y. Umetani, K. Yoshida, Resolved motion rate control of space manipulators with generalized Jacobian matrix, *IEEE Transactions on Robotics and Automation* 5 (3) (1989) 303–314.
- [5] K. Yoshida, N. Sashida, R. Kurazume, Y. Umetani, Modeling of collision dynamics for space free-floating links with extended generalized inertia tensor, in: Proceedings of IEEE International Conference on Robotics and Automation, 1992, pp. 899–904.
- [6] Y. Umetani, K. Yoshida, Workspace and manipulability analysis of space manipulator, *Transactions of the Society of Instrument and Control Engineers* 8 (1) (2001) 1–8.
- [7] K. Yoshida, Practical coordination control between satellite attitude and manipulator reaction dynamics based on computed momentum concept, in: Proceedings of IEEE/RSJ International Conference on Intelligent Robots and Systems, 1994, pp. 1578–1585.
- [8] F. Aghili, Coordination control of a free-flying manipulator and its base attitude to capture and detumble a noncooperative satellite, in: Proceedings of IEEE/RSJ International Conference on Intelligent Robots and Systems, 2009, pp. 2365–2372.
- [9] K. Yoshida, Engineering test satellite VII flight experiments for space robot dynamics and control: theories on laboratory test beds ten years ago, now in orbit, *The International Journal of Robotics Research* 22 (5) (2003) 321–335.
- [10] S. Dubowsky, M. Torres, Path planning for space manipulators to minimize spacecraft attitude disturbances, in: Proceedings of IEEE International Conference on Robotics and Automation, 1991, pp. 2522–2528.
- [11] S. Dubowsky, E. Papadopoulos, The kinematics, dynamics, and control of free-flying and free-floating space robotic systems, *IEEE Transactions on Robotics and Automation* 9 (5) (1993) 531–543.
- [12] D. Nenchev, K. Yoshida, Y. Umetani, Introduction of redundant arms for manipulation in space, in: IEEE International Workshop on Intelligent Robots, 1988, pp. 679–684.

- [13] D. Nenchev, Y. Umetani, K. Yoshida, Analysis of a redundant free-flying space-craft/manipulator system, *IEEE Transactions on Robotics and Automation* 8 (1) (1992) 1–6.
- [14] D. Nenchev, K. Yoshida, P. Vichitkulsawat, M. Uchiyama, Reaction null-space control of flexible structure mounted manipulator systems, *IEEE Transactions on Robotics and Automation* 15 (6) (1999) 1011–1023.
- [15] K. Yoshida, K. Hashizume, D. Nenchev, N. Inaba, M. Oda, Control of a space manipulator for autonomous target capture - ETS-VII flight experiments and analysis, in: Proceedings of AIAA Guidance, Navigation, and Control Conference and Exhibit, 2000, pp. 2000–4376.
- [16] K. Yoshida, K. Hashizume, S. Abiko, Zero reaction maneuver: flight validation with ETS-VII space robot and extension to kinematically redundant arm, in: Proceedings of IEEE International Conference on Robotics and Automation, 2001, pp. 441–446.
- [17] R. Lampariello, J. Heindl, R. Koeppe, G. Hirzinger, Reactionless control for two manipulators mounted on a cable-suspended platform, in: 2006 IEEE/RSJ International Conference on Intelligent Robots and Systems, 2006, pp. 91–97.
- [18] T. Oki, H. Nakanishi, K. Yoshida, Whole-body motion control for capturing a tumbling target by a free-floating space robot, in: Proceedings of IEEE/RSJ International Conference on Intelligent Robots and Systems, 2007, pp. 2256–2261.
- [19] Y. Fukazu, N. Hara, Y. Kanamiya, D. Sato, Reactionless resolved acceleration control with vibration suppression capability for JEMRMS/SFA, in: 2008 IEEE International Conference on Robotics and Biomimetics, 2009, pp. 1359–1364.
- [20] T.-C. Nguyen-Huynh, I. Sharf, Adaptive reactionless motion for space manipulator when capturing an unknown tumbling target, in: 2011 IEEE International Conference on Robotics and Automation, 2011, pp. 4202–4207.
- [21] D. Nenchev, K. Yoshida, Impact analysis and post-impact motion control issues of a free-floating Space robot subject to a force impulse, *IEEE Transactions on Robotics and Automation* 15 (3) (1999) 548–557.
- [22] D. Dimitrov, K. Yoshida, Momentum distribution in a space manipulator for facilitating the post-impact control, in: Proceedings of IEEE/RSJ International Conference on Intelligent Robots and Systems, 2004, pp. 3345–3350.
- [23] S. V. Shah, I. Sharf, A. Misra, Reactionless path planning strategies for capture of tumbling objects in space using a dual-arm robotic system, in: Proceedings of AIAA Guidance, Navigation, and Control Conference, Reston, Virginia, 2013, pp. AIAA 2013–4521.
- [24] D. Hirano, Y. Fujii, S. Abiko, R. Lampariello, K. Nagaoka, K. Yoshida, Simultaneous control for end-point motion and vibration suppression of a space robot based on simple dynamic model, in: Proceedings of IEEE International Conference on Robotics and Automation, 2014, pp. 6631–6637.
- [25] K. Nanos, E. Papadopoulos, Avoiding dynamic singularities in Cartesian motions of free-floating manipulators, *IEEE Transactions on Aerospace and Electronic Systems* 51 (3) (2015) 2305–2318.
- [26] V. F. Romano, F. Cosmi, D. N. Nenchev, A. Rovetta, FRIEND: An extra-vehicular activity retriever telerobotic project, *Space Technology* 15 (3) (1995) 123–131.

- [27] A. Pisculli, L. Felicetti, P. Gasbarri, G. Palmerini, M. Sabatini, A reaction-null/Jacobian transpose control strategy with gravity gradient compensation for on-orbit space manipulators, *Aerospace Science and Technology* 38 (2014) 30–40.
- [28] H. Sone, D. N. Nenchev, On some practical reactionless motion tasks with a free-floating space robot, in: *Proceedings of IEEE International Conference on Robotics and Automation*, 2015, pp. 2836–2841.
- [29] M. Oda, K. Kibe, F. Yamagata, ETS-VII, space robot in-orbit experiment satellite, in: *Proceedings of IEEE International Conference on Robotics and Automation*, Vol. 1, 1997, pp. 739–744.
- [30] M. S. Konstantinov, M. D. Markov, D. N. Nenchev, Kinematic control of redundant manipulators, in: *Proceedings of 11th Int. Symp. Industr. Robots*, 1981, pp. 561–568.
- [31] H. Hanafusa, T. Yoshikawa, Y. Nakamura, Analysis and control of articulated robot arms with redundancy, in: *Preprints 8th Triennial IFAC World Congress* 14:78-83, 1981, pp. 78–83.
- [32] Y. Nakamura, H. Hanafusa, T. Yoshikawa, Task-priority based redundancy control of robot manipulators, *The International Journal of Robotics Research* 6 (2) (1987) 3–15.
- [33] K. Kreutz-Delgado, M. Long, H. Seraji, Kinematic analysis of 7-DOF manipulators, *The International Journal of Robotics Research* 11 (5) (1992) 469–481.
- [34] R. Boudreau, R. Podhorodeski, Singularity analysis of a kinematically simple class of 7-jointed revolute manipulators, *Transactions of the Canadian Society for Mechanical Engineering* 34 (1) (2010) 105–117.
- [35] Y. Nakamura, H. Hanafusa, Inverse kinematic solutions with singularity robustness for robot manipulator control, *Journal of Dynamic Systems, Measurement, and Control* 108 (3) (1986) 163.
- [36] C. Wampler, Manipulator inverse kinematic solutions based on vector formulations and damped least-squares methods, *IEEE Transactions on Systems, Man, and Cybernetics* 16 (1) (1986) 93–101.
- [37] D. Nenchev, Y. Tsumaki, M. Uchiyama, Adjoint Jacobian closed-loop kinematic control of robots, in: *Proceedings of IEEE International Conference on Robotics and Automation*, 1996, pp. 1235–1240.
- [38] D. N. Nenchev, Singularity-consistent parameterization of robot motion and control, *The International Journal of Robotics Research* 19 (2) (2000) 159–182.
- [39] S. K. Agrawal, S. Shirumalla, Planning motions of a dual-arm free-floating manipulator keeping the base inertially fixed, *Mechanism and Machine Theory* 30 (1) (1995) 59–70.
- [40] N. Hara, D. Nenchev, D. Sato, Momentum conserving path tracking through dynamic singularities with a flexible-base redundant manipulator, in: *Proceedings of IEEE/RSJ International Conference on Intelligent Robots and Systems*, 2010, pp. 5392–5397.
- [41] S. Taki, D. Nenchev, Euler angle based feedback control of large eigenaxis rotations in the presence of singularities and model uncertainty, in: *Proceedings of the 13th International Conference on Control, Automation and Systems*, 2013, pp. 34–39.

- [42] E. Aboaf, R. Paul, Living with the singularity of robot wrists, in: Proceedings of IEEE International Conference on Robotics and Automation, 1987, pp. 1713–1717.
- [43] S. Chiaverini, Singularity-robust task-priority redundancy resolution for real-time kinematic control of robot manipulators, *IEEE Transactions on Robotics and Automation* 13 (3) (1997) 398–410.
- [44] S. Chiaverini, B. Siciliano, O. Egeland, Review of the damped least-squares inverse kinematics with experiments on an industrial robot manipulator, *IEEE Transactions on Control Systems Technology* 2 (2) (1994) 123–134.
- [45] D. Nenchev, Tracking manipulator trajectories with ordinary singularities: A null space-based approach, *The International Journal of Robotics Research* 14 (4) (1995) 399–404.
- [46] Y. Tsumaki, D. Nenchev, S. Kotera, M. Uchiyama, Teleoperation based on the adjoint Jacobian approach, *IEEE Control Systems Magazine* 17 (1) (1997) 53–62.
- [47] Y. Tsumaki, S. Kotera, D. Nenchev, M. Uchiyama, Advanced experiments with a teleoperation system based on the SC approach, in: Proceedings of IEEE/RSJ International Conference on Intelligent Robots and Systems, 1998, pp. 1196–1201.
- [48] D. N. Nenchev, Natural motion and singularity-consistent inversion of robot manipulators, in: *Advances in Robot Control*, Springer Berlin Heidelberg, 2007, pp. 9–33.
- [49] D. N. Nenchev, Y. Handa, D. Sato, Natural motion: efficient path tracking with robotic limbs, in: *2010 IEEE/RSJ International Conference on Intelligent Robots and Systems*, 2010, pp. 3483–3488.
- [50] M. Torres, S. Dubowsky, Path-planning for elastically constrained space manipulator systems, in: Proceedings of IEEE International Conference on Robotics and Automation, 1993, pp. 812–817.